

Grain Size in the Class I Protostellar System TMC-1A Constrained with ALMA and VLA Observations

YUSUKE ASO ¹, SATOSHI OHASHI ², HAYU BAOBAB LIU ^{3,4} AND WENRUI XU ⁵

¹*Korea Astronomy and Space Science Institute (KASI), 776 Daedeokdae-ro, Yuseong-gu, Daejeon 34055, Republic of Korea*

²*National Astronomical Observatory of Japan, 2-21-1 Osawa, Mitaka, Tokyo 181-8588, Japan*

³*Physics Department, National Sun Yat-Sen University, Taiwan, Republic of Chinese*

⁴*Center of Astronomy and Gravitation, National Taiwan Normal University, Taipei 116, Taiwan*

⁵*Center for Computational Astrophysics, Flatiron Institute, NY, USA*

ABSTRACT

The disk mass and substructure in young stellar objects suggest that planet formation may start at the protostellar stage through the growth of dust grains. To accurately estimate the grain size at the protostellar stage, we have observed the Class I protostar TMC-1A using the Jansky Very Large Array (VLA) at the Q (7 mm) and Ka (9 mm) bands at a resolution of $\sim 0''.2$ and analyzed archival data of Atacama Large Millimeter/submillimeter Array (ALMA) at Band 6 (1.3 mm) and 7 (0.9 mm) that cover the same spatial scale. The VLA images show a compact structure with a size of ~ 25 au and a spectral index of ~ 2.5 . The ALMA images show compact and extended structures with a spectral index of ~ 2 at the central ~ 40 au region and another index of ~ 3.3 in the outer region. Our SED analysis using the observed fluxes at the four bands suggests one branch with a small grain size of ~ 0.12 mm and another with a grown grain size of ~ 4 mm. We also model polarized dust continuum emission adopting the two grain sizes and compare them with an observational result of TMC-1A, suggesting that the small grain size is preferable to the grown grain size. The small grain size implies gravitational instability in the TMC-1A disk, which is consistent with a spiral-like component recently identified.

Keywords: Circumstellar disks (235) — Circumstellar grains (239) — Protostars (1302) — Low mass stars (2050)

1. INTRODUCTION

The earliest stage of planet formation in protoplanetary disks involves the growth of dust grains (e.g., Testi et al. 2014). The maximum grain size (a_{\max}) in these disks is a fundamental parameter in planet formation, as mechanisms like streaming instability (e.g., Johansen et al. 2014) and pebble accretion (e.g., Liu & Ji 2020) are highly dependent on it (e.g., Drazkowska et al. 2023).

During the formation of gas giant planets, these planets interact with the host disk, generating various substructures through planet-disk interactions (e.g., Paardekooper et al. 2023). These substructures, including rings, gaps, spirals, and crescents, have been both predicted (e.g., Bae et al. 2023) and observed in numerous disks around Class II objects, with rings and gaps being the most common (e.g., Andrews et al. 2018). While many of the planets inferred from disk gaps remain unconfirmed, the successful detection of the planets PDS 70 b and c within the gap of the PDS 70 disk (Kep-

pler et al. 2018; Haffert et al. 2019) strongly supports the link between these substructures and the presence of giant planets.

Similar to Class II disks, substructures have also been observed in some class 0/I disks (Sheehan & Eisner 2017, 2018; Segura-Cox et al. 2020; Lee et al. 2020; Nakatani et al. 2020; Han et al. 2023; Long et al. 2020; Maureira et al. 2024). These discoveries suggest that planet formation could begin as early as the protostellar stage. Examining dust grain growth at this early phase thus provides crucial insights into the initial conditions for planet formation.

Grain size measurement is necessary to verify whether dust grains can grow enough to start planet formation. Diagnosing long-wavelength excess in the spectral energy distribution (SED) has been regarded a useful assessment of grain growth in disks and envelopes around young stellar objects (e.g., Hildebrand 1983; Miyake & Nakagawa 1993; D'Alessio et al. 2001; Draine 2006),

since a dust grain cannot efficiently emit/absorb radiation at wavelengths that are much longer than its diameter. Recent theoretical studies suggest an independent method through polarization due to self-scattering, which is applied to observational results to constrain the grain size in circumstellar disks (e.g., Kataoka et al. 2016, 2017; Ohashi et al. 2018; Bacciotti et al. 2018; Ohashi & Kataoka 2019; Dent et al. 2019; Mori et al. 2019; Lin et al. 2020; Lee et al. 2021; Aso et al. 2021; Lin et al. 2022; Tang et al. 2023). Multi-band polarization observation can constrain the maximum grain size because, in the case of self-scattering, polarization fraction is highest when the maximum grain size is around the observed wavelength over 2π . Overall, longer, centimeter-wavelength observations are preferable for determining whether dust grains have grown to millimeter or centimeter sizes.

Grain size estimation, using the SED or self-scattering method, has been performed only with a limited number of protostellar disks. Zamponi et al. (2024) reported presence of 1-mm-sized grains inside the soot line (within this line, temperature is high enough to sublimate solid amorphous refractory carbon) of the disk in the Class 0 protostellar system IRAS 16293-2422 B using ALMA (1.3 and 3 mm) and VLA (9 and 18 mm) continuum observations at angular resolutions of $\lesssim 0''.2$. The self-scattering method has recently started to be applied to protostellar disks, in addition to the Class I/II disk in HL Tau and more evolved T Tauri disks: the grain size is estimated to be 50-75 μm in the Class 0 protostar HH212 (Lee et al. 2021) and 80-300 μm in the Class I protostar TMC-1A (Aso et al. 2021). Sadavoy et al. (2019) detected polarized continuum emission due to the self-scattering in nine protostellar systems in the Ophiuchus molecular cloud at the 1.3 mm wavelength in ALMA observations at an angular resolution of $\sim 0''.25$.

TMC-1A is the Class I protostar with typical structures: disk, envelope, and outflow (e.g., Aso et al. 2015; Bjerkeli et al. 2016) in the Taurus star forming region at the distance of 141.8 pc (Krolikowski et al. 2021). A previous observational study suggested presence of mm-sized grains in its disk based on line absorption against strong continuum emission at the 1.3 mm wavelength (Harsono et al. 2018). The authors discussed that the high opacity is preferred to high mass of the disk to explain the high optical depth because the TMC-1A disk does not exhibit a substructure as clearly as reported in Class II disks. Meanwhile, previous polarization observations at the 1.3 mm wavelength detected a component due to self-scattering, suggesting a grain size of ~ 0.1 mm (Aso et al. 2021). Multi-band observation is crucial to accurately estimate the grain size in this disk

in the protostellar phase. For this purpose, we have observed TMC-1A using Karl G. Jansky Very Large Array (VLA) in the Q (7 mm) and Ka (9 mm) bands. We also searched for ALMA archival data sets with similar uv -coverage to that of our VLA observations; as a result, ALMA Band 6 and 7 data sets are selected. The visibilities and images in the four bands are analyzed under coherent conditions.

The rest of the paper has the following structure. Section 2 describes the details of our VLA observations and the selected ALMA archival data. Section 3 shows the consistency of the visibilities and images at each band as well as spectral index maps. We analyze the spectral energy distribution at seven positions, showing two solution branches in Section 4.1. Further discussion about preference of the branches are in Section 5. A summary of our results and interpretation is in Section 6. Appendix A shows the details of ALMA data calibration.

2. OBSERVATIONS AND DATA

2.1. VLA Observations

We observed TMC-1A using VLA with the antenna configuration of B in the Q and Ka bands (Project ID: 21B-089). The mapping center was $\alpha(\text{J2000}) = 04^{\text{h}}39^{\text{m}}35^{\text{s}}.010$, $\delta(\text{J2000}) = 25^{\circ}41'45''.500$. The Ka band observations are on 2021 October 23, while the Q band observations are from 2021 October to 2022 January (Oct. 20, 31; Nov. 1, 3, 7, 8; Dec 16; Jan. 3). The on-source observing time is ~ 54 min with the Ka band, while that with the Q band is 3.4 hr. The number of antennas was 27 with the Ka band and 28 with the Q band. The projected baseline length is 216 to 10090 m with the Ka band and 172 to 10175 m with the Q band. Any emission beyond $6''.6$ (~ 920 au) in the Ka band or $4''.5$ (~ 630 au) in the Q band was resolved out by $\gtrsim 63\%$ with the antenna configuration (Wilner & Welch 1994). The bandpass calibrator was J0319+4130, the amplitude (flux) calibrator was 3C147, and the phase (gain) calibrator was J0403+2600.

The observations used 64 spectral windows, covering from ~ 31 to ~ 38 GHz with the Ka band and from ~ 40 to ~ 48 GHz with the Q band, and 4 polarization correlations (RR, RL, LR, and LL). Each spectral window covers $2 \text{ MHz} \times 64 = 128 \text{ MHz}$.

All the imaging procedure was carried out with Common Astronomical Software Applications (CASA), version 6.5.0.15. The visibilities were Fourier transformed and CLEANed with Briggs weighting and a robust parameter of 2.0. The resultant beam sizes and noise levels are describe in each figure in this paper. Furthermore, the coordinates are modified through the CASA task *fixplanet* so that the central position derived from

the 2D Gaussian fitting through the CASA task *imfit* can be aligned between the two different bands. This modification is also applied to the other ALMA archival data so that every map has the same central position. Even though we tried self-calibration for the VLA data using tasks in CASA (*tclean*, *gaincal*, and *applycal*), it did not increase the signal-to-noise ratio, and thus the VLA images in this paper are not self-calibrated. While all maps are primary-beam corrected in this paper, the noise level were measured in emission-free areas before the primary-beam correction. The full width at half power of the primary beam is $\sim 63''$ with the Q band and $\sim 117''$ with the Ka band.

2.2. ALMA Data Reprocessing

We have reprocessed the archival ALMA data taken at Band 6 (2015.1.01415.S and 2018.1.00701.S) and Band 7 (2015.1.01549.S) that the uv -coverages overlapped with those of our VLA observations. Most of these observations adopted quasar J0510+1800 as the absolute flux calibrator. In our calibration procedures, the absolute flux densities of J0510+1800 were referenced from the ALMA Calibrator Grid Survey, the SMA Calibrator List ¹, and in some cases the archival SMA observations. In 2014–2017, the flux density of J0510+1800 rapidly varied with time. For certain epochs of ALMA observations, the rapid flux variability of J0510+1800 might have induced absolute flux inaccuracy. For this reason, these epochs were not used in our imaging process. The details are commented on and summarized in Table 1 in Appendix A.

3. RESULTS

3.1. Visibility profiles

Figure 1 shows comparison of 1D visibility profiles among the ALMA Band 6 and 7 data sets used in this paper, while Figure 2 shows that of the VLA Ka and Q band data sets. Each profile is derived from the visibilities on the 2D uv -plane. The (u, v) coordinates of visibilities are deprojected assuming a geometrically thin disk structure, i.e., shrunk along the disk minor axis by a factor of $\cos i$, where i is the disk inclination angle. The deprojection adopts the disk major axis direction of P.A. = 75° and the inclination angle of $i = 50^\circ$ (Aso et al. 2021). Then, the deprojected visibilities are azimuthally averaged and radially binned to 50 bins on a logarithmic grid from 6 to 6000 $k\lambda$ to derive the 1D profiles.

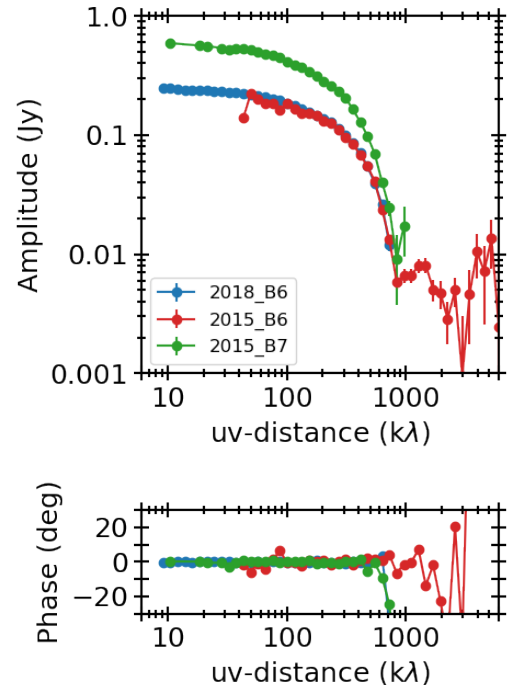


Figure 1. Comparison of 1D visibility profiles among the ALMA Band 6 and 7 data sets used in this paper. Each profile is derived by azimuthally averaging the visibilities on the 2D uv -plane after deprojection with the disk major axis of P.A. = 75° and the disk inclination angle of 50° . The phase reference center is set to be the peak position of each data set.

The ALMA amplitudes show that the two data sets of Band 6 (2015 and 2018) have amplitudes consistent with each other in the common uv -range. This figure also shows that the amplitude significantly decreases in $\gtrsim 200 k\lambda$ in both ALMA bands. Assuming a Gaussian function, the half width at half maximum (HWHM) of 200 $k\lambda$ corresponds to the full width at half maximum (FWHM) of $\sim 0''.5$ in the image domain, which is consistent with different past observations (Aso et al. 2015). In contrast, the VLA amplitudes show a shallower slope in both Ka and Q bands, even though the ALMA and VLA observations share most of the uv -range. This indicates that the VLA continuum emission arises from a central region. The HWHM appears $\sim 500 k\lambda$, and this corresponds to the FWHM of $\sim 0''.2$ of a Gaussian function in the image domain (see also Section 3.2).

3.2. VLA Q and Ka bands

Figure 3 shows the continuum emission observed with our VLA observations in Ka (9 mm) and Q (7 mm) bands, after the primary beam correction. The abscissa and ordinate are the relative coordinates from the Gaus-

¹ SMA Calibrator List: <http://sma1.sma.hawaii.edu/callist/callist.html>.

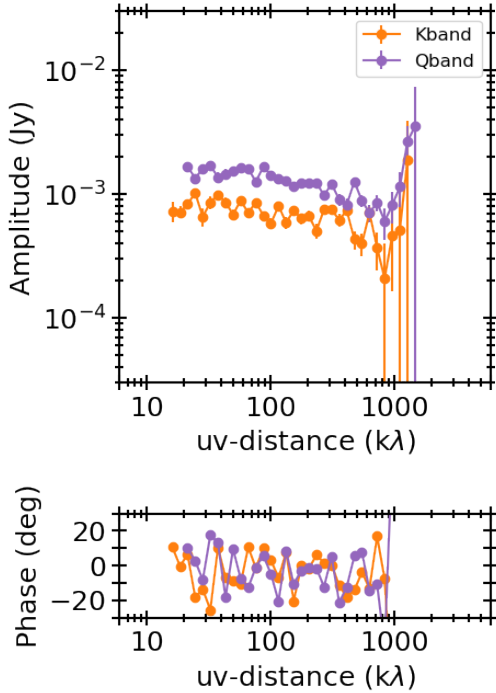
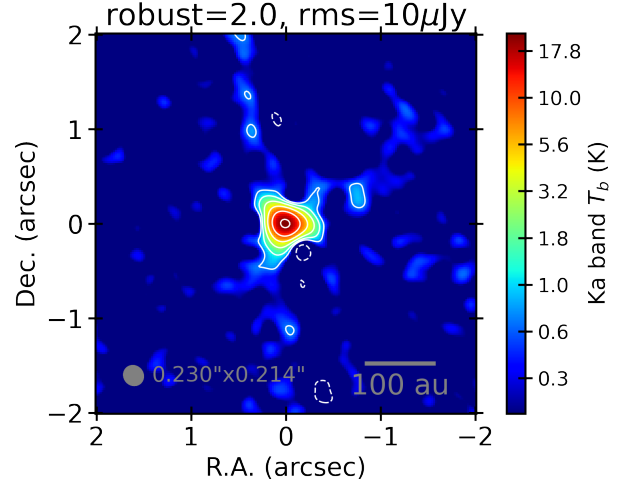


Figure 2. Same as Figure 1 but for the VLA Ka and Q band data sets.

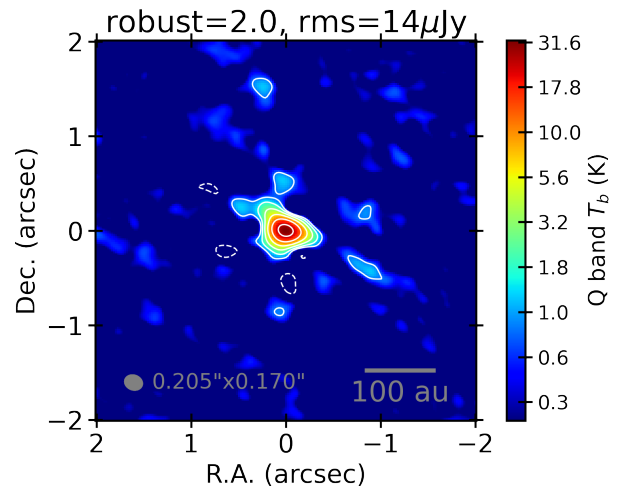
sian center (Section 2). Both images show a compact component at the center and marginally detected components in the north. The northern component traces the eastern side of the blueshifted outflow lobe, which is stronger than the western side of the lobe in the $^{12}\text{CO } J = 2 - 1$ line (Aso et al. 2021). The Ka band image shows the peak intensity of $1.1 \text{ mJy beam}^{-1}$ and the total flux density of 1.8 mJy , while those of the Q band image are $1.8 \text{ mJy beam}^{-1}$ and 3.0 mJy , respectively. The 2D Gaussian fitting provides the deconvolved size of $0''.178 \pm 0''.008 \times 0''.114 \pm 0''.009$ (P.A. = $89^\circ \pm 6^\circ$) with the Ka band image and $0''.179 \pm 0''.005 \times 0''.106 \pm 0''.004$ (P.A. = $75^\circ \pm 2^\circ$) with the Q band image.

3.3. Spectral index map

The combinations of the newly observed VLA Ka and Q band images, as well as the ALMA Band 6 and 7 images from the archive, enable us to measure the spectral index $\alpha = d \ln F_\nu / d \ln \nu$, at each position, where F_ν and ν are the flux density and frequency, respectively. To calculate the index α , the two images must be made from visibilities with the same uv range and have the same synthesized beam size. Hence, in this subsection, we limit the uv range to a common range of $20 - 1000 k\lambda$ to make all the four images. Then, the robust parameter for the CASA task *tclean* is selected



(a) VLA Ka band (9 mm)



(b) VLA Q and (7 mm)

Figure 3. Continuum images in the VLA Ka and Q bands made with the robust parameter of 2.0, after the primary beam correction. The contour levels are in 3σ steps, where 1σ is (a) 10 and (b) $14 \mu\text{Jy beam}^{-1}$. The ellipse at the bottom left corner of each panel is the VLA synthesized beam.

to obtain a synthesized beam size close but smaller than the target resolution $0''.24$: 0.0 for ALMA Band 6, -0.5 for ALMA Band 7, 2.0 for VLA Ka band, and 2.0 for VLA Q band. The synthesized beam size is further tuned to be closer to, but still smaller than, the target resolution by *uv-tapering*: $0''.167 \times 0''.067$ (-79.4°) for ALMA Band 6, $0''.218 \times 0''.065$ (-103.5°) for ALMA Band 7, $0''.076 \times 0''.033$ (133.3°) for VLA Ka band, and $0''.153 \times 0''.066$ (162.4°) for VLA Q band. Finally the synthesized beam size is set to be exactly the target resolution by spatial smoothing through the CASA task *imsmooth*. Using these images at the common resolu-

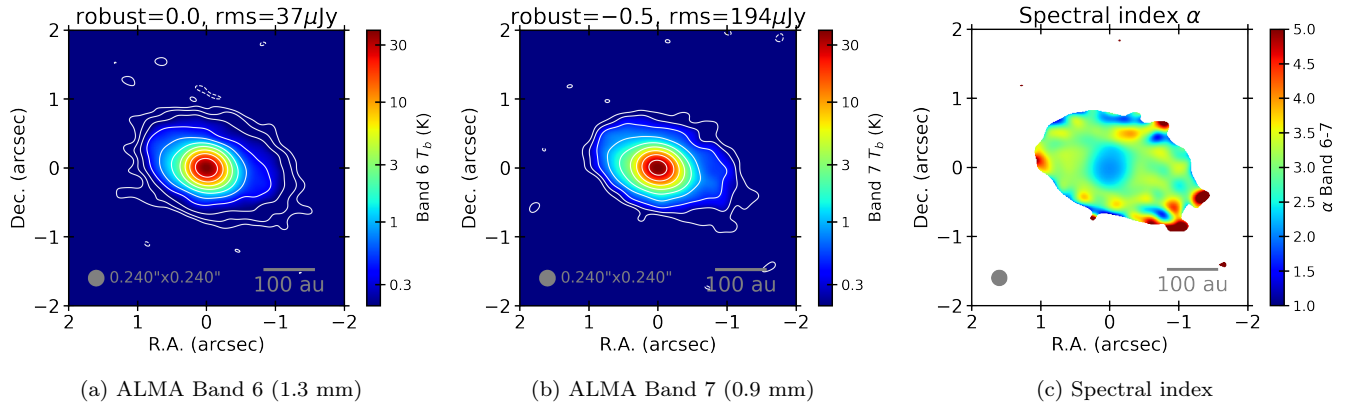


Figure 4. Continuum images in the ALMA Band 6 and 7 made with the same uv range of 20 – 1000 k λ , and the spectral index map made of the two images (panel c). Panels a and b are primary-beam corrected. Contour levels are in the 3σ steps, where 1σ is (a) 0.037 and (b) 0.19 mJy beam $^{-1}$. The spectral index map is masked where the Band 7 continuum emission is below 3σ . The ellipse at the bottom left corner of each panel is the synthesized beam common for all panels ($0''.24 \times 0''.24$). The common beam is achieved by uv -tapering and spatial smoothing after a similar beam is selected by the robust parameter.

tion, the α map is made through the CASA task *im-math*.

Figure 4 shows the ALMA Band 6 and 7 images used to make the α map and the resultant α map. The α values are masked where the Band 7 emission is weaker than the 3σ level. The ALMA Band 6-7 α is closer to 2 at the central ~ 40 au, while it is ~ 3.3 in the outer region (Figure 4c). The index $\alpha \sim 2$ can be confirmed as the same brightness temperature in Band 6 and 7 ~ 32 K in the central region (Figure 4ab). This index indicates that the continuum emission is optically thick, which is consistent with the absorption in the C 18 O and 13 CO $J = 2 - 1$ lines against the strong continuum emission (Harsono et al. 2018).

At the region where the Band 6 and 7 brightness temperatures are $\lesssim 10$ K, the Band 6-7 α is consistent with a spatially uniform value of ~ 3.3 . A common way to interpret the α index is to express it as a function of the optical depth τ and the dust opacity index β as follows:

$$\begin{aligned} \alpha &= \frac{d \ln(B_\nu(T_d)(1 - e^{-\tau_\nu}))}{d \ln \nu} \\ &= \frac{d \ln B_\nu(T_d)}{d \ln \nu} + \frac{\tau_\nu}{e^{\tau_\nu} - 1} \beta, \end{aligned} \quad (1)$$

where B_ν , T_d , and ν are the Planck function, dust temperature, and frequency, respectively. For example, for an assumed dust temperature $T_d \sim 20 - 30$ K, $d \ln B_\nu / d \ln \nu \sim 1.7$ at the middle frequency of our Band 6 and 7 observations, 277 GHz (1.1 mm). In this case, if the Band 6 and 7 observations are (marginally) optically thin ($\tau_\nu < 1$), which is likely the case given the resolved $\lesssim 10$ K dust brightness temperatures, the observed α value would imply that β is approximately between 1.6 ($\tau_\nu \ll 1$) and 2.7 ($\tau_\nu = 1$). This β value is larger than

that of the interstellar dust, which may indicate that the maximum grain size a_{\max} is on the order of 100s μm (β around $\lambda = 1.3$ mm; Pavlyuchenkov et al. 2019). In contrast, $a_{\max} > 1$ mm produces the index of $\beta \lesssim 1.0$ (Pavlyuchenkov et al. 2019).

Figure 5 shows the VLA Ka and Q band images that were used to make the α map and the resultant α map. The α values are masked where the Q band emission is weaker than the 3σ level. The VLA Ka-Q band α is measured only at the central ~ 40 au region at $\alpha \sim 2.5$. Because the brightness temperature in the Ka and Q images is lower than in the ALMA Band 6 and 7 images, the continuum emission is marginally optically thin at Ka and Q bands, if the beam filling factor is unity. The index of the Planck function is $d \ln B_\nu / d \ln \nu \sim 2.0$ at the middle frequency of the our Ka and Q band observations, 31 GHz (0.95 cm), and $T_d > 30$ K. If the optical depth is $\tau_\nu \lesssim 1$, Equation (1) provides β between 0.5 ($\tau_\nu \ll 1$) and 0.9 ($\tau_\nu = 1$), which is much smaller than the β index measured between ALMA Band 6 and 7. This face value of β may imply that the innermost region of the TMC-1A disk has a larger a_{\max} value, although the exact a_{\max} value needs to be examined by the SED fittings that take the beam filling factor and dust scattering opacities (e.g., Liu 2019) into considerations. Such SED analyses are introduced in Section 4.1.

4. ANALYSIS

4.1. Spectral energy distributions

We produced slices of the dust continuum intensity along the major axis of the TMC 1A disk at the observed frequency bands. To avoid cluttering presentations, we only discuss the spectral energy distribution

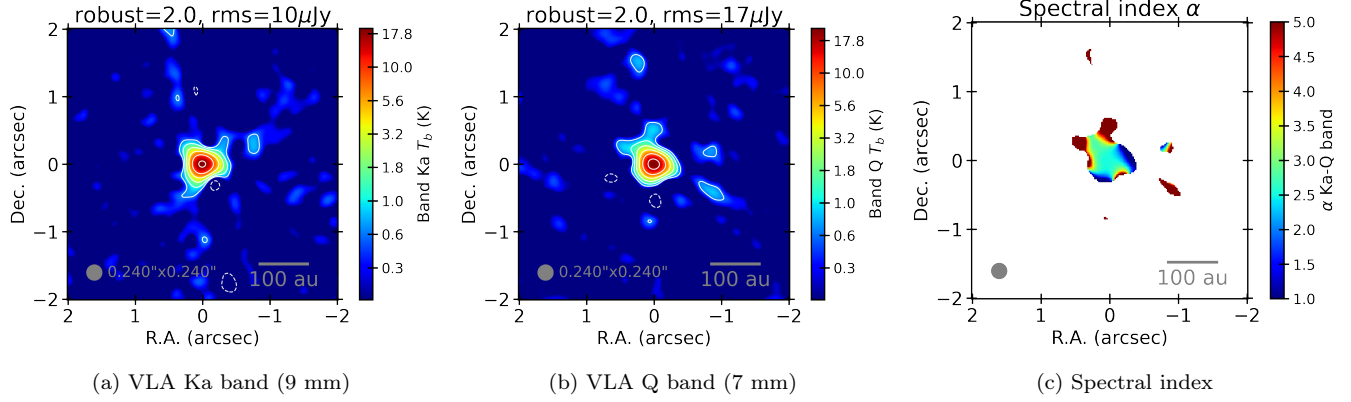


Figure 5. Same as Figure 4 but for the VLA (a) Ka and (b) Q band images, and (c) the spectral index map made of the two images. The 1σ level is (a) 10 and (b) $17 \mu\text{Jy beam}^{-1}$. The spectral index map is masked where the Q band continuum emission is below 3σ .

(SED) models for certain selected offset positions. In addition, instead of sampling the slice at a regular spatial interval, we present more samples on the small spatial scales due to the steeper variations of dust properties (temperature, column density, grain sizes) on smaller spatial scales. Dust properties in the regions between our selected spatial samples can be understood in an interpolated sense.

Our strategy follows that of Liu et al. (2019, 2021) to model the observed flux densities as the contributions of various dust emission components. The exact formulation is as follows:

$$F_\nu = \sum_i F_\nu^i e^{-\sum_j \tau_\nu^{i,j}}, \quad (2)$$

where F_ν^i is the flux density of the dust component i and $\tau_\nu^{i,j}$ is the optical depth of the emission component j that obscures the emission component i .

To take into account the effects of dust self-scattering (e.g., Liu 2019), the flux density of each dust component is evaluated through Equations (11)–(19) in Birnstiel et al. (2018). Limited by the angular resolution, the spatially resolved regions are outside of the water snowline (~ 150 K; e.g., Pollack et al. 1994). Optical constants are, therefore, quoted from the default (i.e., water-ice-coated) DSHARP dust (Birnstiel et al. 2018). To produce the grain-size weighted dust opacities, we assumed a power-law dust (a^q) grain size (a) distribution $n(a)$ between the minimum and maximum grain sizes (a_{\min} , a_{\max}), adopting a nominal $a_{\min} = 10^{-4}$ mm. This modeling tries $q = -2.5$ and $q = -3.5$, which represent the drift-limited and fragmentation limited grain growth, respectively (Birnstiel et al. 2012). As a summary, the free parameters for each dust components are dust temperature (T_{dust}), mass surface density (Σ_{dust}),

maximum grain size a_{\max} , and the beam filling factor f_{beam} when fitting with more than one dust components.

For each selected position, we produced (1) the SED model that assumes uniform dust properties in a line-of-sight (i.e., there is only one dust component), and (2) the SED model with two dust components in a line-of-sight: a surface and a mid-plane dust components. The results of our SED modelings for cases (1) and (2) are discussed in Section 4.2 and 4.3, respectively. Case (2) needs to be considered because using only one dust component cannot reproduce the SEDs at every offset position simultaneously. On the other hand, the number of our independent measurements does not permit assuming more than two dust components in a line-of-sight.

In case (1), the beam filling factor (f_{beam}) is 1.0 everywhere. Due to the degeneracy between dust temperature and f_{beam} , taking f_{beam} as a free parameter does not yield the better reliable fittings.

In case (2), f_{beam} of the surface component is 1 while f_{beam} of the mid-plane component is a free parameter. An additional assumption is that the mid-plane component is obscured by the surface component on the near side, and the surface component on the far side is obscured by both the mid-plane component (taking into account the factor f_{beam}) and the surface component in the near side. In case (2), the assumptions of f_{beam} are hard to avoid due to the limited number of observed frequency bands. Nevertheless, we argued that the assumed 1.0 filling factor at the surface is realistic given the high gas and dust column density in the Class 0/I sources. Since Class 0/I sources may form substructures in the high-density mid-plane (e.g., Sheehan & Eisner 2018; Nakatani et al. 2020; Sheehan et al. 2020; Segura-Cox et al. 2020), given the synthesized beam sizes of the

utilized VLA and ALMA observations, it is possible that the f_{beam} is, in general, less than 1.0 in the mid-plane.

It turned out that the assumptions of $q = -2.5$ and $q = -3.5$ led to qualitatively similar fittings. When fitting with more than one dust components in a line-of-sight, we assumed that the surface and the mid-plane components have the same q and a_{max} values to limit the overall number of free parameters. This assumption is not necessarily realistic. Since the large dust particles may preferentially settle to the disk mid-plane, the surface and mid-plane components may have different a_{max} values. Relaxing these assumptions in principle can yield better fittings, which are however not necessarily scientifically meaningful since it will make the fitting more under-constrained.

Flux densities at centimeter wavelengths could be contributed by the free-free emission from a protostellar jet (Anglada et al. 1998; Liu et al. 2014; Dzib et al. 2015; Tychoniec et al. 2018a; Coutens et al. 2019). We assess the importance of free-free emission based on the archival VLA observations at lower frequencies and found that free-free emission is likely negligible as compared to dust emission in the specific case of TMC1A. The evaluation of the free-free emission is discussed in Section 5.1 in more detail.

4.2. One dust component

The free parameters are optimized using the Markov chain Monte Carlo (MCMC) method through the `emcee` (Foreman-Mackey et al. 2013) package. The number of walkers, steps, and burn-in steps are 60, 1500, and 500, respectively. The fittings occurred to be degenerated: one branch of solutions have $a_{\text{max}} > 1$ mm in general (hereafter the grown dust branch), while the other branch of solutions have $a_{\text{max}} \ll 1$ mm (hereafter the small dust branch). The prior probability functions are uniform but bounded at $a_{\text{max}} \geq 0.5$ mm to focus the fittings on one branch at a time.

Figure 6 shows the grown and small dust branch solutions for the cases with grain size power-law index $q = -2.5$ and $q = -3.5$. With $q = -2.5$, in both the grown and small dust branches, the observed fluxes can be fitted simultaneously at all four frequency bands only at the central location (i.e., offset=0''). Therefore, the single-component dust model with $q = -2.5$ is disfavored. With $q = -3.5$, the grown dust branch can simultaneously fit the measurements at all four frequency bands only in the offset range of $\pm 0''.08$ (~ 11 au). The small dust branch can only simultaneously fit the measurements at all four frequency bands at the central location. In our best-fit models, at the central location,

the a_{max} is $\sim 2\text{--}4$ mm in the grown dust branch, while a_{max} is ~ 0.3 mm in the small dust branch.

At larger offsets, the best-fit models yield spectral indices that are steeper than the observed value between VLA Q and Ka bands. We note that in these cases, the parameter a_{max} did not reliably converge in the MCMC fitting, in particular, when the offsets are comparably larger than $0''.8$ (112 au): the high a_{max} values in the grown dust branch merely reflect that the prior function is not upper-bounded, while the modest a_{max} values in the small dust branch is a result that the a_{max} values of the MCMC samplers were randomly walking in the range of 0–0.5 mm.

These fitting results imply that only one dust component in a line-of-sight cannot sufficiently explain the observations. The good models we obtained at the central location may be coincidence, i.e., they can be biased due to the oversimplified assumption of thermal and density structures.

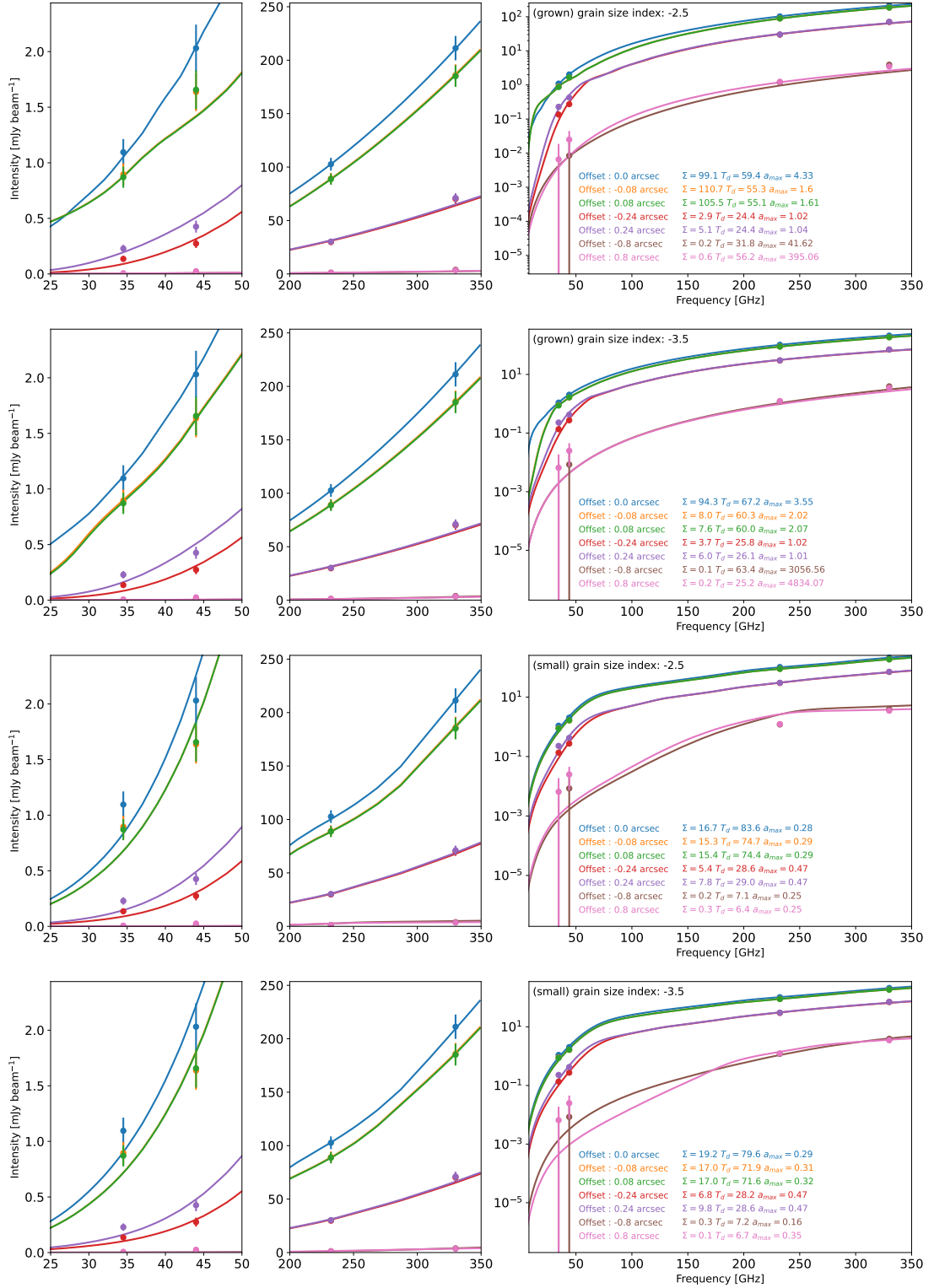


Figure 6. Spectral energy distribution fitting assuming a single DSHARP dust component. The observed intensities are shown by dots that are color-coded by the offset positions. From top to bottom rows, the solid lines show the SED models assuming (1) grown dust branch with $q = -2.5$, (2) grown dust branch with $q = -3.5$, (3) small dust branch with $q = -2.5$, and (4) small dust branch with $q = -3.5$.

4.3. Separating dust mid-plane and surface

We interactively search for the parameters that are consistent with the data. For each line-of-sight, in spite that there are more free parameters than independent measurements, the temperature of the surface component can still be constrained to a certain extent due to the modest optical depth (e.g., implied by the spectral indices between ALMA Band 6 and 7). The dust scattering opacity is very sensitive to a_{\max} , and the attenuation due to the dust scattering opacity can systematically bias the derivation of T_{dust} (e.g., Liu 2019). Nevertheless, in our present case study, this effect is very modest except at the central location. In both grown and small dust branches, with $q = -2.5$ and $q = -3.5$, the radial surface dust-temperature profiles may be approximated by (broken) power-laws: it is either consistent with a ~ -0.7 power-law index, or is consistent with a $-0.6 - -0.7$ power-law index at the inner ~ 30 au radii and a $-0.4 - -0.5$ power-law index at the outer $\sim 30\text{--}100$ au radii (Figure 7).

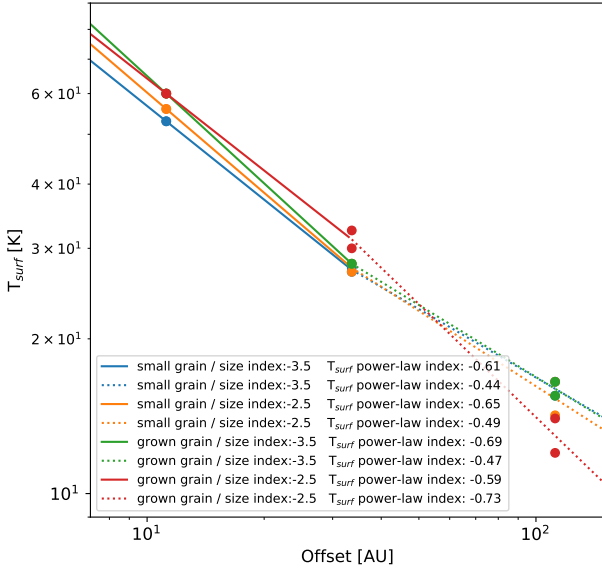


Figure 7. Derived surface dust temperature profiles (see Section 4.3).

Including a mid-plane dust component that is warmer than the surface component and has $f_{\text{beam}} < 1$ can enhance the flux density at 29–48 GHz, as shown in Figure 8. The best-fit models in Figure 8 have $a_{\max} \sim 0.12$ mm in the small dust branch and ~ 4 mm in the grown dust branch as a mean value among the radii. When a small $f_{\text{beam}} < 1$ and a high Σ_{dust} are used, the degree of freedom makes it possible to reproduce the shallow spectral indices observed between the VLA Q and Ka bands.

In the grown dust branch, the relatively high T_{dust} and f_{beam} values are needed for the mid-plane component because the emission from the mid-plane component is strongly attenuated by the scattering opacity of the surface component. The T_{dust} and f_{beam} values for the mid-plane component can be lowered if the grown dust is only present in the disk mid-plane (i.e., the disk surface is in the small dust branch). It seems that the f_{beam} values do not have mirror symmetry with respect to the central position, which may be due to structures in the high-density midplane (e.g., spiral arms or crescent) as reported by Aso et al. (2021) and Xu et al. (2023).

The higher temperature in the disk mid-plane than in the surface and the $-0.6\text{--}0.7$ power-law index in the radial temperature profiles suggest the effect of non-radiative heating mechanisms such as viscous heat dissipation. Similar suggestions have been made in the observational case studies towards the other Class 0/I YSOs (e.g., Liu 2021; Zamponi et al. 2021; Takakuwa et al. 2024), as well as towards TMC-1A (Xu et al. 2023). If this is the case, given certain surface temperature, the mid-plane temperature is positively correlated with the Planck/Rosseland mean opacities and Σ_{dust} (Chiang & Goldreich 1997). The vertical temperature profile of the grown dust branch may not be physical due to the small Planck/Rosseland mean opacities of the grown dust. Given the present observational data, it is difficult to robustly distinguish the grown and small dust branches, as well as telling whether q should be -2.5 or -3.5 . Pinpointing these parameters may require either the observations at more frequency bands or a self-consistent model of dust and gas energetics and heat transportation.

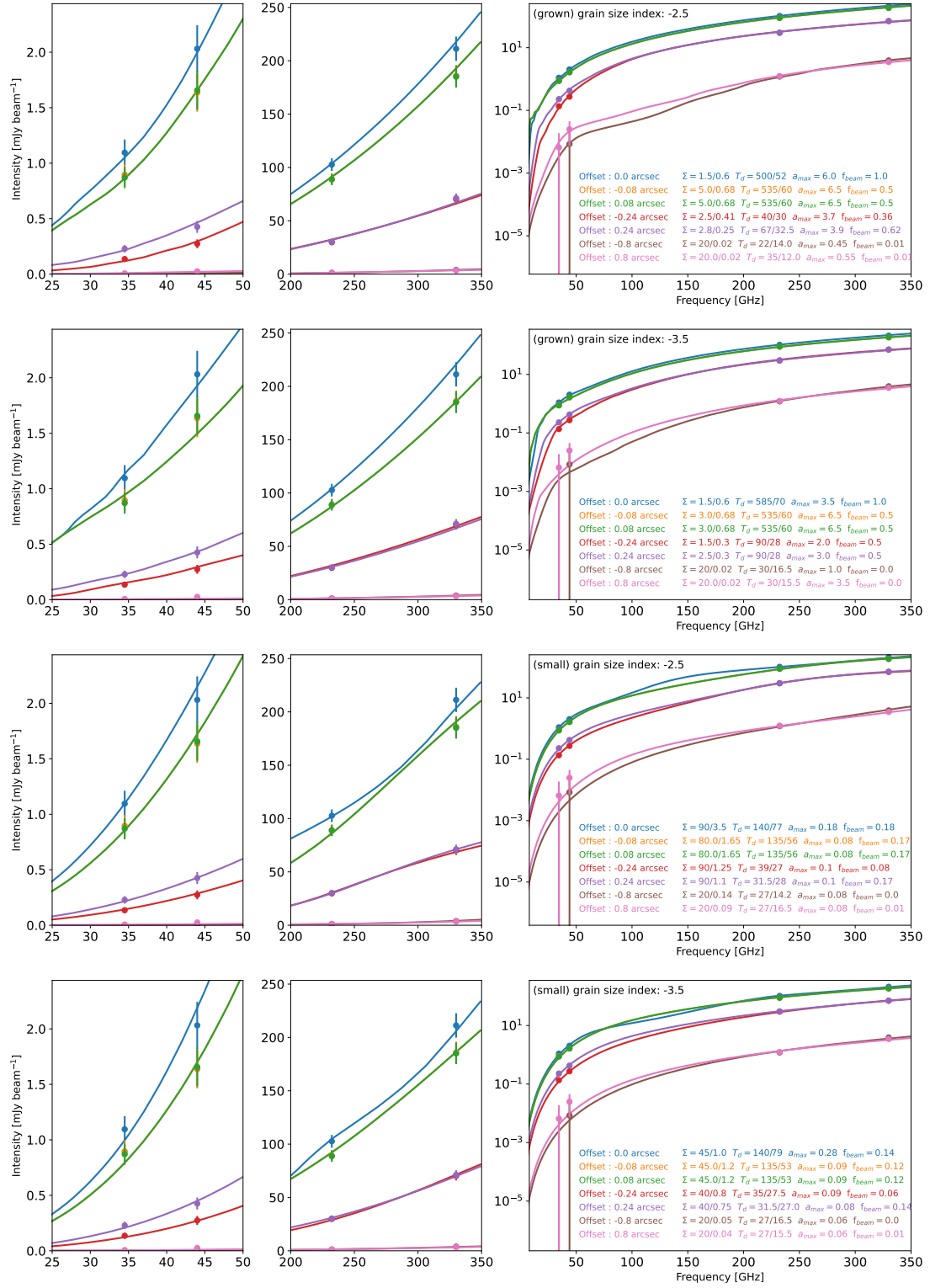


Figure 8. Same as Figure 6 but the SED models assume that there are mid-plane and surface dust components (see Section 4.3).

4.4. Polarization of the two branches

Our SED fitting suggested two branches with small grains ($a_{\max} \sim 0.12$ mm) and grown grains ($a_{\max} \sim 4$ mm) in the protostellar disk in TMC-1A. Another observational constraint may hint at a difference between the two branches. TMC-1A was observed in linearly polarized continuum emission at the 1.3 mm wavelength (Aso et al. 2021), which is independent of the non-polarized fluxes. To take account of this condition, model images of the polarization Stokes I , Q , and U are compared with the results of Aso et al. (2021) in this section.

Our model is based on the fiducial model made for TMC-1A by Xu et al. (2023) because our purpose is not to reproduce the observed intensity distribution in detail, exploring various parameters, but to verify whether the observed polarization signal prefers either of the two branches. While the density and temperature distributions of the original model is calculated from a mass accretion rate and a Toomre Q parameter based on the idea of gravito-viscous heating (Xu 2022), we adopt power-law radial profiles, for simplicity, that approximate the dust surface density and temperature distributions: $\Sigma_{\text{dust}}(R) = 1600 \text{ g cm}^{-2} (R/10 \text{ au})^{-1.96}$ and $T_{\text{dust}} = 185 \text{ K} (R/10 \text{ au})^{-1.27}$, where R is the axial radius. The dust temperature is assumed to be vertically isothermal. The dust density is calculated from the dust surface density and the dust scale height same as the gas scale height determined by the hydrostatic equilibrium. In addition, The dust opacity is calculated with a maximum grain size of a_{\max} using the DSHARP opacity model (Birnstiel et al. 2018). The grain size is spatially uniform. Two maximum grain sizes, 0.12 and 4 mm, are tested to verify the small grain and grown grain branches, respectively. Other related parameters follow the fiducial model, such as the star+disk mass M_{tot} , the disk radius R_d , and the power-law index of the grain size distribution q . Then, the Stokes I , Q , and U intensities in the unit of Jy pixel^{-1} are calculated at 1.3 mm through RADMC-3D (Dullemond et al. 2012) by solving radiative transfer. Finally, the model image is convolved with the same 2D Gaussian beam as that of the observed image in Aso et al. (2021). While the noise level of the observed image is $25 \mu\text{Jy beam}^{-1}$, our model does not include any artificial noise.

Figure 9(a) shows results of the small-grain model in the polarized 1.3-mm continuum emission. The spatial scale and the color range follows Figure 2 of Aso et al. (2021). The model image shows consistent results with the observation: (1) The polarized intensity is detected above $75 \mu\text{Jy beam}^{-1}$ in the central $r \lesssim 50$ au, (2) The polarization fraction is $\sim 1\%$ in the central re-

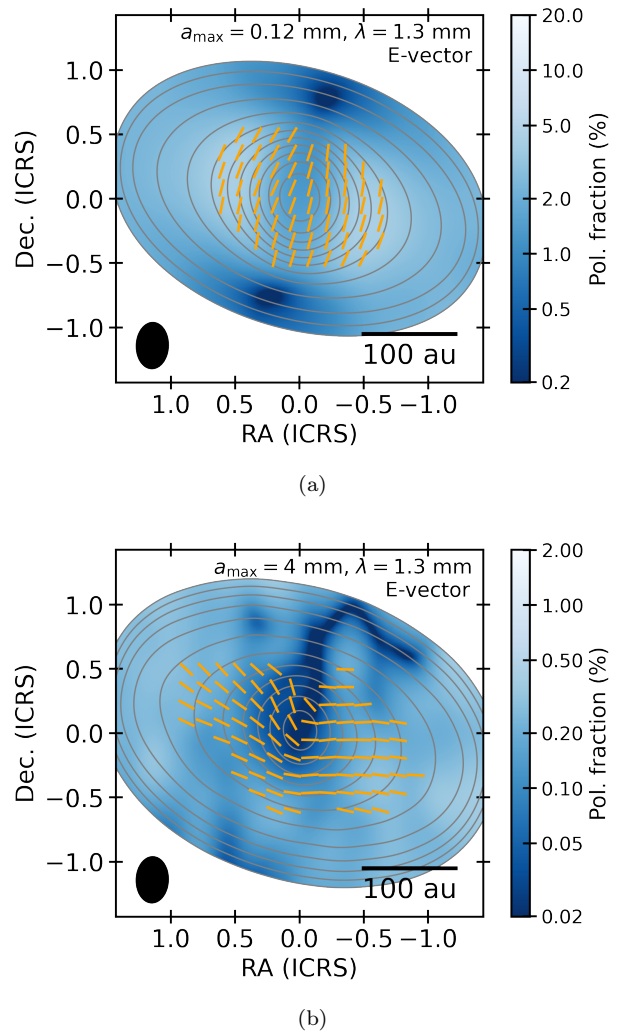


Figure 9. Disk models with maximum grain sizes of (a) 0.12 and (b) 4 mm. The contours show Stokes I , where the contour spacing is 3, 6, 12, 24... $\times 25 \mu\text{Jy beam}^{-1}$; $25 \mu\text{Jy beam}^{-1}$ is the rms noise level in Aso et al. (2021). The polarization fraction is shown at positions where Stokes I is $> 75 \mu\text{Jy beam}^{-1}$. The polarization directions are shown using segments at positions where the polarization intensity is $> 75 \mu\text{Jy beam}^{-1}$ in panel (a) and $> 7.5 \mu\text{Jy beam}^{-1}$ in panel (b). The spatial scale, beam size, and contour levels follow Figure 2 of Aso et al. (2021).

gion, (3) The polarization direction is mainly in the disk minor-axis direction inside the central region, and (4) The Stokes I intensity is consistent except for the peak that is roughly twice higher than the observation. The central strong emission of our model may be attributed to the vertically isothermal temperature, the uniform grain size distribution, or the dust model; however, adjusting Stokes I is beyond the scope of this section, i.e., the comparison of polarized signals.

Figure 9(b) shows results of the grown-grain model. While the spatial scale is the same, the color range is ten times lower than that of Figure 9(a). The Stokes I intensity of this model is similar to that of the small-grain model. The other points are, however, different from those of the observations and the small-grain model: (1) the polarized intensity is below $75 \mu\text{Jy beam}^{-1}$ in the central region, (2) The polarization fraction is $\lesssim 0.05\%$, and (3) The polarization direction is not in the disk minor-axis direction, even if the Stokes Q and U components below the detection level ($75 \mu\text{Jy beam}^{-1}$) are considered.

5. DISCUSSION

5.1. Effect of free-free emission

Fluxes at centimeter wavelengths in protostellar systems could include free-free emission from protostellar jets (Anglada et al. 1998; Dzib et al. 2013; Liu et al. 2014; Dzib et al. 2015; Tychoniec et al. 2018a; Coutens et al. 2019). The NRAO VLA Archive Survey Images Page² shows no detection in a VLA observation toward TMC-1A at the C band (6.1 cm), where free-free emission is expected, with a beam size of $0''.36$ and a sensitivity of $0.07 \text{ mJy beam}^{-1}$. While the sensitivity is ~ 10 times worse than that of Tychoniec et al. (2018a) with a similar beam size. The detected C band fluxes of the protostars in Tychoniec et al. (2018a) are $\gtrsim 0.6 \text{ mJy beam}^{-1}$ if they were located at the distance of TMC-1A. Hence, the existing VLA C band data suggest that the free-free emission in TMC-1A is weaker than other protostars. This little impact of free-free emission is supported by two other evaluation methods in this subsection.

The first method uses the bolometric luminosity. Previous studies suggest the correlation between the free-free emission at 4.1 and 6.4 cm and the bolometric luminosity (Tychoniec et al. 2018b). Using this relation and power-law scaling, Xu (2022) evaluate the contribution of free-free emission at the VLA Ka band. The same scaling can be adopted for TMC-1A. Tychoniec et al. (2018b) show empirical laws of $\log L_{4.1\text{cm}} = (-2.66 \pm 0.06) + (0.91 \pm 0.06) \log L_{\text{bol}}$ and $\log L_{6.4\text{cm}} = (-2.80 \pm 0.07) + (1.00 \pm 0.07) \log L_{\text{bol}}$, where $L_{6.4\text{cm}}$ and $L_{4.1\text{cm}}$ are the luminosity (distance-corrected flux) of free-free emission at each wavelength in the unit of mJy kpc^2 , while L_{bol} is the bolometric luminosity in the unit of L_{\odot} . Assuming the same spectral index from 6.4 to 0.9 cm, the free-free luminosity at 0.9 cm can be estimated as $\log L_{0.9\text{cm}} = (-2.66 \pm 0.06) + (0.6 \pm 0.3) \log L_{\text{bol}}$. Then, the bolometric luminosity of TMC-1A, $2.3 L_{\odot}$

(Ohashi et al. 2023a), and its distance, 141.8 pc, provide the expected free-free flux of $F_{0.9\text{cm}} = 0.18 \pm 0.05 \text{ mJy}$. This flux is an order of magnitude smaller than the actual observed flux, supporting that the Ka band flux is dominated by the dust emission in TMC-1A.

The second method is the continuum morphology. The free-free emission tends to be elongated in the outflow direction in a protostellar system (Tychoniec et al. 2018a). Our results show that the elongated direction of the Ka band emission in TMC-1A is P.A. = $89^{\circ} \pm 6^{\circ}$ (Section 3.2) based on the 2D Gaussian fitting. This direction is closer to the disk major axis (P.A. = 75° ; Aso et al. 2021) than the disk minor axis or outflow/jet direction. This morphology supports that the VLA Ka band traces dust emission in TMC-1A.

5.2. Grain size in other protostellar disks

The grain size measurements in protostellar disks are limited to a few targets yet (Section 1). Previous observational studies suggest several tens μm for the disk of the Class 0 protostar HH212 (Lee et al. 2021), 100 μm for the outside and 1 mm for the inside of the soot line ($r = 10 \text{ au}$) in the disk of the Class 0 protostar IRAS 16293-2422 B (Zamponi et al. 2024), $> 1 \text{ mm}$ for the late Class I protostar WL 17 (Han et al. 2023, Hashimoto et al. in prep.), $> 1 \text{ mm}$ for the disk of the Class I/II protostar HL Tau (Zhang et al. 2023), and $> 3 \text{ mm}$ for the outer region in the disk of Class I/II protostar DG Tau (Ohashi et al. 2023b). Our results correspond to the middle of these Class 0 and I protostars in terms of the evolutionary phase. While a natural interpretation may be that dust grains grow to $\sim 100 \mu\text{m}$ during the Class 0 phase and grow further to $> 1 \text{ mm}$ during the Class I phase, concluding the time scale of grain growth requires to resolve the grain size distribution in protostellar disks, evaluate the evolutionary stage of each protostellar system more precisely, and increase the sample of protostellar disks where the grain size is estimated through polarization and non-polarization methods using multiple wavelengths and considering the optical depth.

5.3. Disk mass

With the multi-layer model, the small grain branch has larger surface densities than the grown grain branch by around an order of magnitude. In other words, the preference of the small grain branch means that a higher disk mass is preferred. Previously Harsono et al. (2018) argued that a disk mass high enough to explain an absorption feature in the $\text{C}^{18}\text{O } J = 2 - 1$ line should induce a non-axisymmetric structure in the disk. While the authors declined the possibility of such a high disk mass because the TMC-1A disk does not show a non-axisymmetric structure obviously, recent observations

² <https://www.vla.nrao.edu/astro/nvas/>

have identified a one-armed spiral-like structure as a residual from axisymmetric disk models in the ALMA Bands 6 and 7 (Aso et al. 2021; Xu et al. 2023). Furthermore, Xu et al. (2023) has explained the pitch angle of the spiral by gravitational instability of the TMC-1A disk. Aso et al. (2021) also show that the pitch angle is consistent with the ratio between the infall velocity and the rotational velocity along the spiral. These recent results support the possibility of a disk mass high enough to induce gravitational instability. Gravitational instability in the Class I phase could also be the reason of the small grain size, as the turbulence driven by gravitational instability suppresses collisional growth of typical dust grains (Xu & Armitage 2023; Xu et al. 2023). As a result, planet formation may need to wait until the infall-driven gravitational instability stops, and may occur during the transition between Class I and II phases. This is consistent with a recent survey result that protostellar disks appear to show less substructures (Ohashi et al. 2023a) than more evolved protoplanetary disks (Andrews et al. 2018).

5.4. Complementarity of analyses

The comparison of the polarized emission between the observation and our two models (Section 4.4) suggests that the small grain branch ($a_{\max} \sim 0.12$ mm) is preferable to the grown grain branch ($a_{\max} \sim 4$ mm). The two branches show different behaviors in a frequency range between the VLA Q band and ALMA Band 6, which has not been observed yet with the coherent condition. Other frequencies higher than the ALMA Band 7 may also be required to trace the temperature distribution more directly. In the case of self-scattering, the polarization fraction as a function of the observed wavelength can constrain the maximum grain size (e.g., Kataoka et al. 2017). Hence, new observations at different wavelengths but with the coherent condition, in polarized and non-polarized emission, are necessary to further constrain the grain size in this protostar at the Class I stage, where planet formation is expected to start.

The model-independent SED fitting is complementary to analytic disk models, such as the one built by Xu et al. (2023). On one hand, our SED fitting demonstrates that even multi-wavelength dust continuum observations that spatially resolve the disk is insufficient to uniquely pin down dust properties. On the other hand, analytic disk models rely on the assumption of a constant gas-to-dust mass ratio throughout a disk. This can be achieved when the dust grains remain small and thus are dynamically well coupled with the gas in the disk. The consistency between our model-independent SED fitting (the small grain branch) and the analytic

disk model of Xu et al. (2023) implies that this assumption is reasonable, in TMC-1A, and validates the physical assumptions of the analytic disk model. After such validation, an analytic disk model has strengths that it can fit the entire disk structures with free parameters as few as those of the model-independent SED fitting. In contrast, analytic disk models may work only in diffuse regions with small grains when there are azimuthally (a)symmetric local concentrations of grown grains (e.g., ring or crescent; Liu et al. 2024) that are largely different from a rather smooth disk assumed in analytic disk models. Even in such a case, the model-independent SED fitting provides complementary diagnostics of dust growth and migration. It is thus important to develop both analyses together with new observations.

6. CONCLUSIONS

We have observed the Class I protostar TMC-1A using the VLA at the Q (7 mm) and Ka (9 mm) bands and analyzed archival data of ALMA at Bands 6 (1.3 mm) and 7 (0.9 mm) at an angular resolution of $\sim 0''.2$ to accurately estimate the grain size in the protostellar disk. The main results are summarized below.

1. The VLA images show a compact structure, in both bands, with a size of $\sim 0''.18$ (25 au) and a spectral index of ~ 3 . The ALMA images show an extended structure with a size of $\sim 2''$ (300 au), as well as a compact component. The spectral index calculated from the ALMA images is ~ 2 at the central ~ 40 au, while it is ~ 3 in the outer region.
2. We searched for models that reproduce the spectral energy distribution derived from the four images at seven different positions. As a result, our SED fitting revealed two branches that are degenerate: a small grain branch with $a_{\max} \sim 0.1$ mm and a grown grain branch with $a_{\max} \sim 4$ mm.
3. We also made model images of the polarization fraction and direction and compared the model result with an observed polarization result. The small grain branch provides Stokes I intensity, polarization direction, and polarization fraction more consistent with the observation than the grown grain branch.
4. The ~ 0.1 -mm grain size is an intermediate value among the present measurements of the grain size in protostellar systems: Several tens to 100 μm in systems younger than TMC-1A, while > 1 -3 mm in systems more evolved than TMC-1A. The small

grain also implies gravitational instability, suggested by a spiral-like component recently identified. Gravitational instability may suppress planet formation until the transition from the Class I phase to the Class II phase.

This paper makes use of the following ALMA data: ADS/JAO.ALMA#2015.1.01415.S, ADS/JAO.ALMA#2015.1.01549.S, and ADS/JAO.ALMA#2018.1.00701.S. ALMA is a partnership of ESO (representing its member states), NSF (USA) and NINS (Japan), together with NRC (Canada), MOST and ASIAA (Taiwan), and KASI (Republic of Korea), in cooperation with the Republic of Chile. The Joint ALMA Observatory is operated by ESO, AUI/NRAO and NAOJ. The National Radio Astronomy Observatory is a facility of the National Science Foundation operated under cooperative agreement by Associated Universities, Inc. H.B.L. is supported by the National Science and Technology Council (NSTC) of Taiwan (Grant Nos. 111-2112-M-110-022-MY3).

Facilities: ALMA, VLA

Software: [astropy](#) (Astropy Collaboration et al. 2013, 2018), [Numpy](#) (van der Walt et al. 2011), [CASA](#) (v6.5; McMullin et al. 2007), [emcee](#) (Foreman-Mackey et al. 2013), [corner](#) (Foreman-Mackey 2016), [RADMC-3D](#) (Dullemond et al. 2012),

APPENDIX

A. COMMENTS ON ALMA DATA CALIBRATION

A.1. 2015.1.01415.S

There were three epochs of observations (Table 1). The pointing and phase referencing centers for the target source TMC-1A were $\alpha(\text{J2000}) = 04^{\text{h}}39^{\text{m}}35^{\text{s}}.2$, $\delta(\text{J2000}) = +25^{\circ}41'44''.27$. The observations employed five spectral windows that the central frequency and bandwidths (in GHz units) are spw0: 230.538 / 0.117, spw1: 231.469 / 1.875, spw2: 217.055 / 0.469, spw3: 219.561 / 0.117, and spw4: 220.399 / 0.117, respectively. The ALMA data archive only provided the calibration scripts for the observations taken on 2015 October 23 and 30 since the observations taken on 2015 October 16 failed to pass quality assurance 2 (QA2). We manually re-calibrated all three epochs of observations using the CASA software package.

The complex gain calibrator adopted in this project (J0440+2728) was relatively faint at the observing frequency (~ 50 mJy). For this reason, all the five spectral windows were combined to maximize the S/N ratios when deriving the complex gain solutions. The residual gain phase errors appeared large in all three epochs of observations after the basic calibrations. Both the faintness of the complex gain calibrator and the compromised quality of the gain phase solutions led to the uncertain gain amplitude solutions for the spectral windows spw0, 2, 3, and 4. We did not find a way that can suppress the amplitude errors without systematically biasing the absolute flux scales. Hence, only the data taken from spw1, which have low amplitude errors, is used in the spectral index analyses.

We calibrated the absolute flux scales at the central frequency of spw1 by referencing the interpolated flux densities of J0510+1800 measured from the ALMA Calibrator Grid Survey and the SMA Calibrator List. Specifically, the ALMA Bands 3, 6, and 7 observations and the SMA 225 GHz observations taken on 2015 October 15 were interpolated to calibrate the absolute flux of the observations taken on 2015 October 16; the ALMA Bands 3 and 7 observations taken on 2015 October 23 were interpolated to calibrate the observations taken on the same date; the ALMA Bands 3, 6, and 7 observations and the SMA 225 GHz observations taken on 2015 November 01 were interpolated to calibrate the observations taken on 2015 October 30. After the absolute flux calibration, the bootstrapped flux densities of the

complex gain calibrator J0440+2720 on 2015. Oct. 16, 23, and 30 are ($F_{217.06 \text{ GHz}} = 0.075 \text{ Jy}$, $F_{231.47 \text{ GHz}} = 0.056 \text{ Jy}$), ($F_{217.06 \text{ GHz}} = 0.058 \text{ Jy}$, $F_{231.47 \text{ GHz}} = 0.050 \text{ Jy}$), and ($F_{217.06 \text{ GHz}} = 0.058 \text{ Jy}$, $F_{231.47 \text{ GHz}} = 0.051 \text{ Jy}$), respectively. Due to the rapid flux variability of J0510+1800, only the absolute flux scale of the observations taken on 2015 October 23 was considered highly reliable. Nevertheless, given that the bootstrapped flux density of J0440+2728 on 2015 October 30 was closely consistent with that on 2015 October 23, the absolute flux scaling in this epoch of observations is likely accurate, although this does not rule out the possibility that the consistency of the J0440+2728 flux densities on different dates was merely a coincidence. We do not have a firm mechanism to assess the absolute flux accuracy of the 2015 October 16 observations, although the bootstrapped flux density of J0440+2728 at 231 GHz appeared reasonable.

To suppress the residual phase errors, self-calibration was performed with several iterations only for gain phase using the CASA `gaincal` and `clean` tasks. Limited by the signal-to-noise ratio of the target source, the reasonable minimum solution interval (i.e., without being subject to massive data flaggings) was ‘per scan’. The intra-scan phase dispersion of the observations taken on 2015 October 16 was large, which cannot be fully removed by applying the ‘per scan’ gain phase self-calibration solutions. To avoid biasing the intensity due to phase decoherence, the long-baseline data taken from the observations on 2015 October 16 were not used. The self-calibration procedures inevitably flagged some long-baseline data. For all three epochs of observations, we manually flagged some antennae that were located at relatively remote stations to suppress the effects of phase decoherence further.

A.2. 2015.1.01549.S

There was an epoch of observations taken on 2016 July 26 (Table 1). The pointing and phase referencing centers for the target source TMC-1A were $\alpha(\text{J2000}) = 04^{\text{h}}39^{\text{m}}35^{\text{s}}.2$, $\delta(\text{J2000}) = +25^{\circ}41'44''44$. The observations employed five spectral windows that the central frequency and bandwidths (in GHz units) are spw0: 329.986 / 1.875, spw1: 340.724 / 0.059, spw2: 339.352 / 0.059, spw3: 329.340 / 0.059, and spw4: 330.598 / 0.059, respectively. The absolute flux, passband, and complex gain calibrators are the quasar J0510+1800. We manually re-calibrated the observations using the CASA software package. When deriving the complex gain solutions, all the five spectral windows were combined to maximize the S/N ratios.

We calibrated the absolute flux scales by referencing the ALMA Calibrator Grid Survey measurements on J0510+1800. In the ALMA Calibrator Grid Survey, 91.5/103.5 GHz measurements were carried out two days before the observations on TMC-1A, and 343.5 GHz measurements were carried out two days after the observations on TMC-1A. These measurements were interpolated to the central frequency of spw0. Due to the rapid flux variability of J0510+1800, we expect the uncertainty of the absolute flux after calibration to be $\sim 30\%$. We do not think this epoch of ALMA observations can yield reliable intra-band spectral indices and thus only used the data taken at spw0 in our scientific analyses. There were no complementary SMA observations on J0510+1800 on proximate dates, which prevents us precisely assessing the absolute flux and spectral index errors.

The residual gain phase errors were large after the basic calibrations. To suppress the phase errors, self-calibration was performed with several iterations only for gain phase using the CASA-`gaincal` and `clean` tasks. Only the broadband continuum window spw0 was used with the per-integration solution interval of 6.05 seconds.

A.3. 2018.1.00701.S

This was a polarization track carried out on 2018 November 21. Details of the data calibration can be found from Aso et al. (2021). The absolute flux calibrator J0510+1800 was covered by the ALMA Calibrator Grid Survey on 2018 November 21 (at multiple frequencies). Therefore, the absolute flux scale of this track is very reliable.

REFERENCES

- Andrews, S. M., Huang, J., Pérez, L. M., et al. 2018, ApJL, 869, L41, doi: [10.3847/2041-8213/aaf741](https://doi.org/10.3847/2041-8213/aaf741)
- Anglada, G., Villuendas, E., Estalella, R., et al. 1998, AJ, 116, 2953, doi: [10.1086/300637](https://doi.org/10.1086/300637)
- Aso, Y., Kwon, W., Hirano, N., et al. 2021, ApJ, 920, 71, doi: [10.3847/1538-4357/ac15f3](https://doi.org/10.3847/1538-4357/ac15f3)
- Aso, Y., Ohashi, N., Saigo, K., et al. 2015, ApJ, 812, 27, doi: [10.1088/0004-637X/812/1/27](https://doi.org/10.1088/0004-637X/812/1/27)
- Astropy Collaboration, Robitaille, T. P., Tollerud, E. J., et al. 2013, A&A, 558, A33, doi: [10.1051/0004-6361/201322068](https://doi.org/10.1051/0004-6361/201322068)

Table 1. Summary of the ALMA archival data

Date (UTC)	Band	PWV ^a (mm)	<i>uv</i> -range (meter)	Mean freq. (bandwidth) (GHz / GHz)	Flux calibrator ^b (Jy, —)	Self-cal. solint ^c (second)
Project Code: 2015.1.01415.S (c.f. Bjerkeli et al. 2016; Harsono et al. 2018)						
2015 Oct. 16	6	2	64–16105	231.5 / 1.875	$F_{223.81\text{GHz}} = 2.53, \alpha = -0.26$	~ 50
2015 Oct. 23	6	0.6	80–14720	231.5 / 1.875	$F_{223.81\text{GHz}} = 2.71, \alpha = -0.28$	~ 50
2015 Oct. 30	6	0.4	79–15186	231.5 / 1.875	$F_{223.80\text{GHz}} = 3.22, \alpha = -0.24$	~ 50
Project Code: 2015.1.01549.S (c.f. Harsono et al. 2021)						
2016 Jul. 26	7	0.4	14–1051	330.0 / 1.875	$F_{334.00\text{GHz}} = 1.32, \alpha = -0.47$	6.05
Project Code: 2018.1.00701.S (c.f. Aso et al. 2021)						
2018 Nov. 21	6	0.8	14–1256	233.0 / 2.000	$F_{224.11\text{GHz}} = 1.68, \alpha = -0.50$	6.05

^aMean precipitable water vapour.

^bThe flux density of the absolute flux calibrator J0510+1800, at a certain frequency, that we assumed during the data reprocessing, shown with the spectral index α of the calibrator at the frequency. It is derived based on referencing to either the ALMA calibrator grid survey or the SMA Calibrator List.

^cSolution interval for gain phase self-calibration. The intervals of ~ 50 and 6.05 second correspond to ‘per scan’ and ‘per integration’, respectively.

- Astropy Collaboration, Price-Whelan, A. M., Sipőcz, B. M., et al. 2018, *AJ*, 156, 123, doi: [10.3847/1538-3881/aabc4f](https://doi.org/10.3847/1538-3881/aabc4f)
- Bacciotti, F., Girart, J. M., Padovani, M., et al. 2018, *ApJL*, 865, L12, doi: [10.3847/2041-8213/aadf87](https://doi.org/10.3847/2041-8213/aadf87)
- Bae, J., Isella, A., Zhu, Z., et al. 2023, in *Astronomical Society of the Pacific Conference Series*, Vol. 534, *Protostars and Planets VII*, ed. S. Inutsuka, Y. Aikawa, T. Muto, K. Tomida, & M. Tamura, 423, doi: [10.48550/arXiv.2210.13314](https://doi.org/10.48550/arXiv.2210.13314)
- Birnstiel, T., Klahr, H., & Ercolano, B. 2012, *A&A*, 539, A148, doi: [10.1051/0004-6361/201118136](https://doi.org/10.1051/0004-6361/201118136)
- Birnstiel, T., Dullemond, C. P., Zhu, Z., et al. 2018, *ApJL*, 869, L45, doi: [10.3847/2041-8213/aaf743](https://doi.org/10.3847/2041-8213/aaf743)
- Bjerkeli, P., van der Wiel, M. H. D., Harsono, D., Ramsey, J. P., & Jørgensen, J. K. 2016, *Nature*, 540, 406, doi: [10.1038/nature20600](https://doi.org/10.1038/nature20600)
- Chiang, E. I., & Goldreich, P. 1997, *ApJ*, 490, 368, doi: [10.1086/304869](https://doi.org/10.1086/304869)
- Coutens, A., Liu, H. B., Jiménez-Serra, I., et al. 2019, *A&A*, 631, A58, doi: [10.1051/0004-6361/201935340](https://doi.org/10.1051/0004-6361/201935340)
- D’Alessio, P., Calvet, N., & Hartmann, L. 2001, *ApJ*, 553, 321, doi: [10.1086/320655](https://doi.org/10.1086/320655)
- Dent, W. R. F., Pinte, C., Cortes, P. C., et al. 2019, *MNRAS*, 482, L29, doi: [10.1093/mnrasl/sly181](https://doi.org/10.1093/mnrasl/sly181)
- Draine, B. T. 2006, *ApJ*, 636, 1114, doi: [10.1086/498130](https://doi.org/10.1086/498130)
- Drażkowska, J., Bitsch, B., Lambrechts, M., et al. 2023, in *Astronomical Society of the Pacific Conference Series*, Vol. 534, *Protostars and Planets VII*, ed. S. Inutsuka, Y. Aikawa, T. Muto, K. Tomida, & M. Tamura, 717, doi: [10.48550/arXiv.2203.09759](https://doi.org/10.48550/arXiv.2203.09759)
- Dullemond, C. P., Juhasz, A., Pohl, A., et al. 2012, *RADMC-3D: A multi-purpose radiative transfer tool*, *Astrophysics Source Code Library*, record ascl:1202.015. <http://ascl.net/1202.015>
- Dzib, S. A., Loinard, L., Mioduszewski, A. J., et al. 2013, *ApJ*, 775, 63, doi: [10.1088/0004-637X/775/1/63](https://doi.org/10.1088/0004-637X/775/1/63)
- Dzib, S. A., Loinard, L., Rodríguez, L. F., et al. 2015, *ApJ*, 801, 91, doi: [10.1088/0004-637X/801/2/91](https://doi.org/10.1088/0004-637X/801/2/91)
- Foreman-Mackey, D. 2016, *The Journal of Open Source Software*, 1, 24, doi: [10.21105/joss.00024](https://doi.org/10.21105/joss.00024)
- Foreman-Mackey, D., Hogg, D. W., Lang, D., & Goodman, J. 2013, *PASP*, 125, 306, doi: [10.1086/670067](https://doi.org/10.1086/670067)
- Haffert, S. Y., Bohn, A. J., de Boer, J., et al. 2019, *Nature Astronomy*, 3, 749, doi: [10.1038/s41550-019-0780-5](https://doi.org/10.1038/s41550-019-0780-5)
- Han, I., Kwon, W., Aso, Y., Bae, J., & Sheehan, P. 2023, *ApJ*, 956, 9, doi: [10.3847/1538-4357/acf853](https://doi.org/10.3847/1538-4357/acf853)
- Harsono, D., Bjerkeli, P., van der Wiel, M. H. D., et al. 2018, *Nature Astronomy*, 2, 646, doi: [10.1038/s41550-018-0497-x](https://doi.org/10.1038/s41550-018-0497-x)
- Harsono, D., van der Wiel, M. H. D., Bjerkeli, P., et al. 2021, *A&A*, 646, A72, doi: [10.1051/0004-6361/202038697](https://doi.org/10.1051/0004-6361/202038697)
- Hildebrand, R. H. 1983, *QJRAS*, 24, 267

- Johansen, A., Blum, J., Tanaka, H., et al. 2014, in *Protostars and Planets VI*, ed. H. Beuther, R. S. Klessen, C. P. Dullemond, & T. Henning, 547–570, doi: [10.2458/azu_uapress_9780816531240-ch024](https://doi.org/10.2458/azu_uapress_9780816531240-ch024)
- Kataoka, A., Muto, T., Momose, M., Tsukagoshi, T., & Dullemond, C. P. 2016, *ApJ*, 820, 54, doi: [10.3847/0004-637X/820/1/54](https://doi.org/10.3847/0004-637X/820/1/54)
- Kataoka, A., Tsukagoshi, T., Pohl, A., et al. 2017, *ApJL*, 844, L5, doi: [10.3847/2041-8213/aa7e33](https://doi.org/10.3847/2041-8213/aa7e33)
- Kepler, M., Benisty, M., Müller, A., et al. 2018, *A&A*, 617, A44, doi: [10.1051/0004-6361/201832957](https://doi.org/10.1051/0004-6361/201832957)
- Krolikowski, D. M., Kraus, A. L., & Rizzuto, A. C. 2021, *AJ*, 162, 110, doi: [10.3847/1538-3881/ac0632](https://doi.org/10.3847/1538-3881/ac0632)
- Lee, C.-F., Li, Z.-Y., & Turner, N. J. 2020, *Nature Astronomy*, 4, 142, doi: [10.1038/s41550-019-0905-x](https://doi.org/10.1038/s41550-019-0905-x)
- Lee, C.-F., Li, Z.-Y., Yang, H., et al. 2021, *ApJ*, 910, 75, doi: [10.3847/1538-4357/abe53a](https://doi.org/10.3847/1538-4357/abe53a)
- Lin, Z.-Y. D., Li, Z.-Y., Yang, H., et al. 2020, *MNRAS*, 496, 169, doi: [10.1093/mnras/staa1499](https://doi.org/10.1093/mnras/staa1499)
- . 2022, *MNRAS*, 512, 3922, doi: [10.1093/mnras/stac753](https://doi.org/10.1093/mnras/stac753)
- Liu, B., & Ji, J. 2020, *Research in Astronomy and Astrophysics*, 20, 164, doi: [10.1088/1674-4527/20/10/164](https://doi.org/10.1088/1674-4527/20/10/164)
- Liu, H. B. 2019, *ApJL*, 877, L22, doi: [10.3847/2041-8213/ab1f8e](https://doi.org/10.3847/2041-8213/ab1f8e)
- . 2021, *ApJ*, 914, 25, doi: [10.3847/1538-4357/abf8b6](https://doi.org/10.3847/1538-4357/abf8b6)
- Liu, H. B., Galván-Madrid, R., Forbrich, J., et al. 2014, *ApJ*, 780, 155, doi: [10.1088/0004-637X/780/2/155](https://doi.org/10.1088/0004-637X/780/2/155)
- Liu, H. B., Mérand, A., Green, J. D., et al. 2019, *ApJ*, 884, 97, doi: [10.3847/1538-4357/ab391c](https://doi.org/10.3847/1538-4357/ab391c)
- Liu, H. B., Tsai, A.-L., Chen, W. P., et al. 2021, *ApJ*, 923, 270, doi: [10.3847/1538-4357/ac31b9](https://doi.org/10.3847/1538-4357/ac31b9)
- Liu, H. B., Muto, T., Konishi, M., et al. 2024, *arXiv e-prints*, arXiv:2402.02900, doi: [10.48550/arXiv.2402.02900](https://doi.org/10.48550/arXiv.2402.02900)
- Long, F., Pinilla, P., Herczeg, G. J., et al. 2020, *ApJ*, 898, 36, doi: [10.3847/1538-4357/ab9a54](https://doi.org/10.3847/1538-4357/ab9a54)
- Maureira, M. J., Pineda, J. E., Liu, H. B., et al. 2024, *A&A*, 689, L5, doi: [10.1051/0004-6361/202451166](https://doi.org/10.1051/0004-6361/202451166)
- McMullin, J. P., Waters, B., Schiebel, D., Young, W., & Golap, K. 2007, in *Astronomical Society of the Pacific Conference Series*, Vol. 376, *Astronomical Data Analysis Software and Systems XVI*, ed. R. A. Shaw, F. Hill, & D. J. Bell, 127
- Miyake, K., & Nakagawa, Y. 1993, *Icarus*, 106, 20, doi: [10.1006/icar.1993.1156](https://doi.org/10.1006/icar.1993.1156)
- Mori, T., Kataoka, A., Ohashi, S., et al. 2019, *ApJ*, 883, 16, doi: [10.3847/1538-4357/ab3575](https://doi.org/10.3847/1538-4357/ab3575)
- Nakatani, R., Liu, H. B., Ohashi, S., et al. 2020, *ApJL*, 895, L2, doi: [10.3847/2041-8213/ab8eaa](https://doi.org/10.3847/2041-8213/ab8eaa)
- Ohashi, N., Tobin, J. J., Jørgensen, J. K., et al. 2023a, *ApJ*, 951, 8, doi: [10.3847/1538-4357/acd384](https://doi.org/10.3847/1538-4357/acd384)
- Ohashi, S., & Kataoka, A. 2019, *ApJ*, 886, 103, doi: [10.3847/1538-4357/ab5107](https://doi.org/10.3847/1538-4357/ab5107)
- Ohashi, S., Kataoka, A., Nagai, H., et al. 2018, *ApJ*, 864, 81, doi: [10.3847/1538-4357/aad632](https://doi.org/10.3847/1538-4357/aad632)
- Ohashi, S., Momose, M., Kataoka, A., et al. 2023b, *ApJ*, 954, 110, doi: [10.3847/1538-4357/ace9b9](https://doi.org/10.3847/1538-4357/ace9b9)
- Paardekooper, S., Dong, R., Duffell, P., et al. 2023, in *Astronomical Society of the Pacific Conference Series*, Vol. 534, *Protostars and Planets VII*, ed. S. Inutsuka, Y. Aikawa, T. Muto, K. Tomida, & M. Tamura, 685, doi: [10.48550/arXiv.2203.09595](https://doi.org/10.48550/arXiv.2203.09595)
- Pavlyuchenkov, Y., Akimkin, V., Wiebe, D., & Vorobyov, E. 2019, *MNRAS*, 486, 3907, doi: [10.1093/mnras/stz1046](https://doi.org/10.1093/mnras/stz1046)
- Pollack, J. B., Hollenbach, D., Beckwith, S., et al. 1994, *ApJ*, 421, 615, doi: [10.1086/173677](https://doi.org/10.1086/173677)
- Sadavoy, S. I., Stephens, I. W., Myers, P. C., et al. 2019, *ApJS*, 245, 2, doi: [10.3847/1538-4365/ab4257](https://doi.org/10.3847/1538-4365/ab4257)
- Segura-Cox, D. M., Schmiedeke, A., Pineda, J. E., et al. 2020, *Nature*, 586, 228, doi: [10.1038/s41586-020-2779-6](https://doi.org/10.1038/s41586-020-2779-6)
- Sheehan, P. D., & Eisner, J. A. 2017, *ApJL*, 840, L12, doi: [10.3847/2041-8213/aa6df8](https://doi.org/10.3847/2041-8213/aa6df8)
- . 2018, *ApJ*, 857, 18, doi: [10.3847/1538-4357/aaae65](https://doi.org/10.3847/1538-4357/aaae65)
- Sheehan, P. D., Tobin, J. J., Federman, S., Megeath, S. T., & Looney, L. W. 2020, *ApJ*, 902, 141, doi: [10.3847/1538-4357/abbad5](https://doi.org/10.3847/1538-4357/abbad5)
- Takakuwa, S., Saigo, K., Kido, M., et al. 2024, *arXiv e-prints*, arXiv:2401.08722, doi: [10.48550/arXiv.2401.08722](https://doi.org/10.48550/arXiv.2401.08722)
- Tang, Y.-W., Dutrey, A., Koch, P. M., et al. 2023, *ApJL*, 947, L5, doi: [10.3847/2041-8213/acc45b](https://doi.org/10.3847/2041-8213/acc45b)
- Testi, L., Birnstiel, T., Ricci, L., et al. 2014, in *Protostars and Planets VI*, ed. H. Beuther, R. S. Klessen, C. P. Dullemond, & T. Henning, 339–361, doi: [10.2458/azu_uapress_9780816531240-ch015](https://doi.org/10.2458/azu_uapress_9780816531240-ch015)
- Tychoniec, Ł., Tobin, J. J., Karska, A., et al. 2018a, *ApJ*, 852, 18, doi: [10.3847/1538-4357/aa9980](https://doi.org/10.3847/1538-4357/aa9980)
- . 2018b, *ApJS*, 238, 19, doi: [10.3847/1538-4365/aaceae](https://doi.org/10.3847/1538-4365/aaceae)
- van der Walt, S., Colbert, S. C., & Varoquaux, G. 2011, *Computing in Science and Engineering*, 13, 22, doi: [10.1109/MCSE.2011.37](https://doi.org/10.1109/MCSE.2011.37)
- Wilner, D. J., & Welch, W. J. 1994, *ApJ*, 427, 898, doi: [10.1086/174195](https://doi.org/10.1086/174195)
- Xu, W. 2022, *ApJ*, 934, 156, doi: [10.3847/1538-4357/ac7b94](https://doi.org/10.3847/1538-4357/ac7b94)
- Xu, W., & Armitage, P. J. 2023, *ApJ*, 946, 94, doi: [10.3847/1538-4357/acb7e5](https://doi.org/10.3847/1538-4357/acb7e5)
- Xu, W., Ohashi, S., Aso, Y., & Liu, H. B. 2023, *ApJ*, 954, 190, doi: [10.3847/1538-4357/aced4c](https://doi.org/10.3847/1538-4357/aced4c)

Zamponi, J., Maureira, M. J., Liu, H. B., et al. 2024, *A&A*,
682, A56, doi: [10.1051/0004-6361/202244628](https://doi.org/10.1051/0004-6361/202244628)
Zamponi, J., Maureira, M. J., Zhao, B., et al. 2021,
MNRAS, 508, 2583, doi: [10.1093/mnras/stab2657](https://doi.org/10.1093/mnras/stab2657)

Zhang, S., Zhu, Z., Ueda, T., et al. 2023, *ApJ*, 953, 96,
doi: [10.3847/1538-4357/acdb4e](https://doi.org/10.3847/1538-4357/acdb4e)